

Multi-Sensor Matching with HyperNetworks

Eli Passov

Faculty of Computer Science
Bar-Ilan University
Ramat-Gan, Israel

elipassov@gmail.com

Nathan S. Netanyahu

Faculty of Computer Science
Bar-Ilan University
Ramat-Gan, Israel

Yosi Keller

Faculty of Engineering
Bar-Ilan University
Ramat-Gan, Israel

Abstract

Hypernetworks are models that generate or modulate the weights of another network. They provide a flexible mechanism for injecting context and task conditioning and have proven broadly useful across diverse applications without significant increases in model size. We leverage hypernetworks to improve multimodal patch matching by introducing a lightweight descriptor-learning architecture that augments a Siamese CNN with (i) hypernetwork modules that compute adaptive, per-channel scaling and shifting and (ii) conditional instance normalization that provides modality-specific adaptation (e.g., visible vs. infrared, VIS-IR) in shallow layers. This combination preserves the efficiency of descriptor-based methods during inference while increasing robustness to appearance shifts. Trained with a triplet loss and hard-negative mining, our approach achieves state-of-the-art results on VIS-NIR and other VIS-IR benchmarks and matches or surpasses prior methods on additional datasets, despite their higher inference cost. To spur progress on domain shift, we also release GAP-VIR, a cross-platform (ground/aerial) VIS-IR patch dataset with 500K pairs, enabling rigorous evaluation of cross-domain generalization and adaptation. We make our code publicly available at ¹

1. Introduction

Patch matching is a fundamental task in computer vision with numerous applications, including image registration [81, 84], image retrieval [14, 54], and simultaneous localization and mapping (SLAM) [18, 64]. The patch matching task involves determining whether two image patches originate from the same physical area of interest. In multimodal patch matching, patches come from different modalities, such as RGB and near-infrared (NIR). Multimodal patch

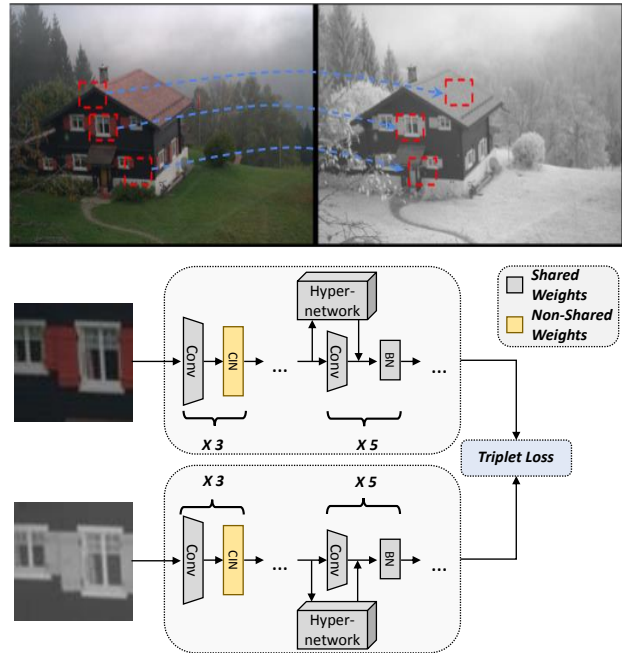


Figure 1. Top: Patch matching between visible (grayscale) and NIR images. Bottom: The proposed hypernetwork-based Siamese CNN, where each branch encodes patches into descriptors. Most weights are shared; deeper layers include convolutions, hypernetwork modules, and batch normalization (BN), while shallow layers use convolutions and conditional instance normalization (CIN) for modality-specific adaptation. A symmetric triplet loss trains the network to learn discriminative descriptors.

matching is used in medical imaging [69] and multisensor image alignment [31]. Modal differences are challenging because the relationship between pixel intensities and the appearance of objects and boundaries varies across modalities. However, these differences make using a network pre-trained on large RGB datasets (e.g., ImageNet [12]) challenging—if not impractical—for multimodal patch match-

¹https://anonymous.4open.science/r/multisensor_hypnet-6EE1.

ing.

Earlier works [1, 2, 10, 17, 46] employed classical feature extraction methods, such as the Scale-Invariant Feature Transform (SIFT), Difference of Gaussians (DoG), or Gabor filters, to create meaningful patch features known as descriptors. Applying metrics such as Euclidean distance to pairs of descriptors enabled determining whether two patches match. Recent methods replace classical feature extractors with deep convolutional neural networks (CNNs) [4, 5, 7, 16, 82] to improve the quality of descriptors. Many works use Siamese CNNs [32], sharing the architecture and weights between the two modalities. Others use pseudo-Siamese [7] CNNs, where the architecture is shared but all or some weights are learned independently for each modality. Descriptor networks are trained using various losses based on Euclidean distance, such as hinge loss [65] or triplet loss [6, 28, 82]. Some works [50, 73, 82] utilize hard negative mining, which continually selects the hardest non-matching patches for training. Besides descriptor learning, some methods employ similarity learning (often called metric learning) [3, 21, 91]. In these works, patches from both modalities are typically processed jointly by a single CNN to determine if they match. Furthermore, some works [38, 56, 85, 86, 89] propose architectures with additional layers and branches that connect to and draw from intermediate feature extraction layers. Although similarity-based methods have achieved favorable results in recent years, using them for inference is less practical [34, 51] due to their higher computational complexity, as discussed in Section 2.2.

In this work, we present a new *descriptor learning* approach to multimodal patch matching, which enhances the Siamese network for feature extraction using two key components. First, we introduce a hypernetwork [19] module that captures contextual information for each channel. An encoder-decoder network then computes dynamic scaling and shifting from this context. Second, we introduce modality-specific context via Conditional Instance Normalization (CIN) [15], originally used for style transfer. We show that applying CIN modules in the shallow layers of a feature extraction network allows the model to more flexibly adapt to different modalities. The introduction of modality-based components converts a fully Siamese network into a pseudo-Siamese network, where nearly all weights, except for a small fraction, are shared between the two modalities. We demonstrate how these additions enhance the performance of widely used descriptor learning architectures for multimodal patch matching. We apply both modules as illustrated in Fig. 1. In the shallow layers, CIN is applied to enable modality-specific adaptation. Hypernetwork blocks are introduced in the deeper layers, where they enrich the shared feature context. We train the Siamese network with a triplet loss [28] combined with

hard negative mining [50]. This setup achieves state-of-the-art (SOTA) results on the VIS-NIR [3] dataset as well as other common benchmarks. In addition, we conduct ablation studies to analyze the contribution of each proposed module and to compare alternative backbones, including ResNet-18 [25], ViT [13], and Swin [44].

Finally, given our results on previously used datasets, we observe that recent work has reached saturation. The lack of new multimodal patch datasets hinders algorithm development and the study of key challenges, notably domain transfer and domain adaptation. To address this, we introduce the **Ground Aerial Patch Vis-IR** (GAP-VIR) dataset (details in Appendix A), containing 500K pairs of matched and unmatched VIS-IR patches from cross-platform imagery (ground-based and aerial). GAP-VIR uniquely enables testing of cross-modal and cross-platform training, as well as evaluating cross-platform adaptation. Our research offers the following key contributions:

- A novel lightweight hypernetwork module infuses global context into feature extraction networks, thereby improving descriptor learning methods.
- The proposed CIN modules improve multimodal matching accuracy by infusing modality-specific context into the network.
- We achieve state-of-the-art results on multimodal patch matching with the proposed approach.
- GAP-VIR, a new cross-platform multimodal (VIS-IR) patch-matching dataset, is introduced to facilitate future research.

2. Related Work

Before CNN-based approaches, patch matching primarily relied on handcrafted, appearance-invariant features. Keller et al. [35] aligned gradient maxima for affine registration through iterative optimization. A similar approach [36] detected false correspondences and adaptively reweighted them using directional similarity. Irani et al. [31] used directional derivative magnitudes as robust descriptors and optimized matching through a coarse-to-fine correlation strategy. Netanyahu et al. [52] employed iterative matching of multiresolution wavelet features for large-scale image registration, using the partial Hausdorff distance for robust correspondence. Lemoigne et al. [41] developed a modular framework for evaluating multitemporal and multisensor registration, integrating diverse features, similarity measures, and optimization strategies. Other works proposed modified SIFT descriptors to enhance geometric invariance and local discriminability. Chen et al. [10] introduced a symmetric SIFT descriptor that is scale and rotation invariant. Ma et al. [49] developed a mirror-invariant variant, and Hasan et al. [24] improved spatial resolution through gradient thresholding and sub-windowing. Kupfer et al. [40] proposed an efficient SIFT-based algorithm for

subpixel registration that filters outliers by mode seeking over keypoint scale ratios, rotation differences, and vertical shifts. Beyond SIFT-based techniques, Aguilera et al. [1] used DoG-based keypoints and edge-oriented histograms that capture shape and contour information, later refined with log-Gabor filters [2]. This approach was refined in [2] by using log-Gabor filters to compute the descriptors. Zhu et al. [95] used log-Gabor filters with multichannel auto-correlation to detect interest points and construct a rotation-invariant descriptor. The self-similarity descriptor by Shechtman et al. [63] is computed per patch, image, or video, and corresponding pairs are compared to identify matches. Kim et al. [37] extended this idea to a dense adaptive self-correlation descriptor that measures similarity between randomly sampled patches within a local support window. Ye et al. [84] further addressed nonlinear radiometric and geometric distortions using steerable-filter descriptors based on first- and second-order gradients.

Siamese networks extract feature representations of two inputs in parallel through shared weights and are widely used in descriptor learning. Simo-Serra et al. [65] utilized the same CNN for both modalities, coupled with a hinge loss that maximizes the distance between non-matching pairs. Other works [5, 6, 48, 75, 82] use a triplet loss [28], which also minimizes the distance of matching pairs. Aguilera et al. [4] introduced the quadruplet loss, where all distances between the features of two sets of matching pairs are included in a loss function that minimizes or maximizes them depending on whether the pairs match or not. Ben-Baruch et al. [7] used a hybrid approach of Siamese and pseudo-Siamese networks, sharing only some of their weights. Other works [50, 73, 82] used hard negative mining, where negative samples are selected for hinge or triplet losses. Zhou et al. [94] combined hard negative mining with continual learning to obtain rotation-invariant features. Kumar et al. [39] proposed a global loss that minimizes the mean distance of matching features, maximizes the mean distance of non-matching features, and minimizes the variance within both groups.

Moreshet et al. [51] added a spatial pyramid pooling layer on top of the backbone and a transformer layer with learned positional embeddings to better capture spatial feature relationships. Tian et al. [74] introduced a second-order similarity regularization to enforce similarity between distances of different patch pairs. The same authors [75] conducted an analysis of the gradient with L_2 and dot-product distances. They applied a regularization term to the positive descriptor distances to tackle the impact of image intensity variability on the descriptors. The authors used a hybrid dot-product and L_2 similarity measure in the main loss function. They also employed a filter response normalization (FRN) layer followed by a threshold linear unit (TLU), both introduced in [66]. Han et al. [21] pro-

posed a convolutional Siamese network that extracts features from two patches, concatenates them, and passes the result into a classification MLP (Multi-Layer Perceptron). Zagoruyko [91] and Aguilera [3] considered three architectures: Siamese, pseudo-Siamese, and two-channel networks. In the hybrid approach of Quan et al. [56], the two inputs are passed through separate branches of a Siamese CNN. The same authors [57] also proposed extracting the concatenation, subtraction, and multiplication of the output features of each modality for every layer. Each of the three relational features is passed through a small channel attention network and trained using an LMCL loss. Ko et al. [38] proposed a similarity-learning approach in which two modality-specific networks first convert inputs into the opposite modality. Then, for each modality, the original and converted inputs are passed into a Siamese network to produce a pair of feature vectors, which are used to compute a similarity score. In a series of works, Yu et al. [85, 87, 89] first applied channel attention blocks for feature extraction, then used an encoder-decoder architecture to regularize and enhance the extracted features, and finally introduced a cross-spectral attention network on top of the Siamese feature-extraction network.

Multimodal frameworks such as MINIMA [60] and MatchAnything [26] shift focus from per-pair similarity networks toward large-scale modality-invariant pretraining. These approaches achieve cross-modal generalization by leveraging synthetic or diverse multimodal datasets. Yu et al. [88] proposed a hybrid descriptor- and similarity-learning approach trained with hard-negatively mined samples. Zhang et al. [92, 93] used a quadruplet network, passing patches through two Siamese branches and two pseudo-Siamese branches before concatenating the outputs. To further enhance feature representation, they incorporated Squeeze-and-Excitation (SE) [30], along with either a transformer or Coordinate Attention (CA) [29] for channel attention, in processing intermediate feature maps. Transformer-based cross-modal matchers such as XoFTR [76] and modality-unifying networks for VIS-IR re-identification [90] highlight the role of attention in bridging spectral appearance gaps. Our work complements these approaches by focusing on lightweight architectural improvements for VIS-IR descriptor learning.

On the dataset side, there are additional multisensor datasets such as msGFM [20], a cross-modal ship re-identification benchmark [80], and large-scale RGB-D datasets for reconstruction [79]. In addition, Ran et al. [58] introduced IR500K, a large-scale aggregation of VIS-IR pairs from multiple sources that serves as the foundation for our GAP-VIR dataset.

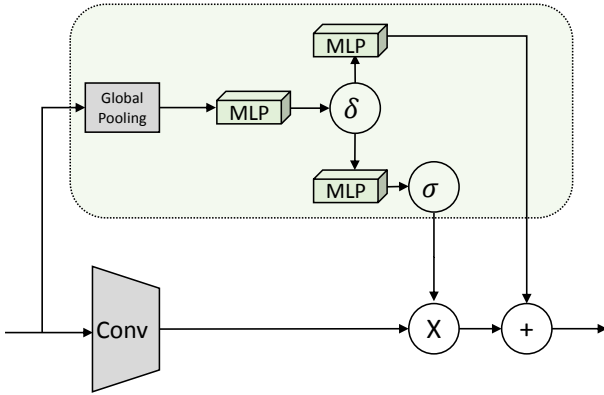


Figure 2. **Hypernetwork module.** The architecture of the hypernetwork: the convolution input is passed through global pooling, followed by fully connected nonlinear layers that produce the scaling and shifting factors. These factors are applied to the convolution output after being replicated across spatial dimensions.

2.1. Hypernetworks

Hypernetworks (introduced in [19]) are used across a wide range of problems, and their architectures and implementation details vary widely depending on the application. For example, [77] uses a hypernetwork to adjust classifier weights based on an embedding produced by another network for multi-source adaptation to unseen domains. In [47], a hypernetwork conditioned on a single input of the target network adapts its weights to improve performance in image classification and 3D reconstruction tasks. Other applications include semantic segmentation [53], implicit neural representations [11, 67], 3D shape reconstruction [42], and continual learning [78] across diverse domains. A comprehensive review and taxonomy of hypernetworks are provided in [9].

2.2. Descriptor Learning vs. Similarity-Based Methods for Patch Matching

Patch matching methods can be broadly categorized into descriptor-learning and similarity-based approaches, which differ substantially in computational cost. When matching patches between two groups of n samples, descriptor learning requires running network inference n times per group to extract feature vectors. After extraction, the pairwise distances between all descriptors from both groups are computed to perform matching, with a worst-case complexity of $O(n^2)$, which can be reduced to $O(n \log n)$ using efficient nearest-neighbor search algorithms, such as kd-trees. In contrast, similarity-based methods require running neural network inference for all $O(n^2)$ matching scores. As a result, descriptor learning is generally more scalable and practical for large datasets and real-time applications.

Table 1. Hypernetwork module architecture.

Part	Module	Output size
Input		$C_{in} \times H \times W$
Bottleneck	Global pooling FC	C_{in} $\frac{C_{in}}{8}$
Scaling	FC + Sigmoid	C_{out}
Shifting	FC	C_{out}

3. Patch Matching using Hyper-Networks

We propose a patch-matching scheme based on a hypernetwork architecture that improves matching accuracy and robustness to appearance variations. Our solution is a descriptor-learning method built on a convolutional Siamese neural network. Given a pair of visual and infrared patches, \mathbf{x}_1 and \mathbf{x}_2 , respectively, the network produces corresponding descriptor vectors, \mathbf{d}_1 and \mathbf{d}_2 , respectively, as illustrated in Fig. 1. Patch matching is determined by the distance between the descriptor vectors.

The Siamese backbone, described in Section 3.1, is convolutional and shares most weights between branches, except for a few components. The hypernetwork modules, detailed in Section 3.2, are added to the deeper layers of the network to enable image-adaptive parameter learning that responds dynamically to appearance variations between the visual and IR images. We train the network using a triplet margin loss, detailed in Section 3.3.

3.1. Network Architecture

The proposed Siamese network is shown in Fig. 1 and Table 2. It consists of eight convolutional layers, chosen to ensure a fair comparison with previous SOTA methods [51].

Batch normalization (BN) is used in deeper layers, while conditional instance normalization (CIN) is applied in the first three layers. The CIN blocks are not weight-shared between the Siamese branches. Breaking weight symmetry allows modality-specific adaptation to the distinct characteristics of visible and IR patches.

The hypernetwork modules are integrated on top of the last five convolutional layers. This design enhances the network’s ability to handle appearance variations between objects in visual and NIR patches. Within the Siamese network, all weights are shared between the visible and NIR branches, except for the CIN block parameters. The effectiveness of the CIN and hypernetwork modules is validated through an ablation study (Section 5.4).

Table 2. CNN architecture used in Hyp-Net: a convolutional backbone followed by convolutional layers with hypernetwork modules, ending with a fully connected head. Input size: 64×64 patch. Conv: 3×3 convolution; Hyp(Conv): hypernetwork module with a 3×3 convolution. Each layer ends with a GELU nonlinearity [27].

Layer	Channels	Stride	Dilation
Conv+CIN+GELU	32	1	1
Conv+CIN+GELU	32	2	1
Conv+CIN+GELU	64	1	2
Hyp(Conv)+BN+GELU	64	2	1
Hyp(Conv)+BN+GELU	128	1	2
Hyp(Conv)+BN+GELU	128	2	1
Hyp(Conv)+BN+GELU	128	1	1
Hyp(Conv)+BN+GELU	128	1	1
Flatten	8192		
Dropout (0.5)	8192		
FC	128		

3.2. Hypernetwork Module

The hypernetwork module H , illustrated in Fig. 2, computes the per-channel scaling and shifting factors applied to the convolutional layer output $L(\mathbf{x})$. Given $\mathbf{x} \in \mathbb{R}^{C_{in} \times H_{in} \times W_{in}}$ as input, L produces the output feature map $\mathbf{y} \in \mathbb{R}^{C_{out} \times H_{out} \times W_{out}}$. The input \mathbf{x} to L is also provided to the hypernetwork module.

3.3. Loss Function

The network is trained using the triplet margin loss [28]:

$$\mathcal{L}(d_a, d_p, d_n) = \max(0, D(d_a, d_p) - D(d_a, d_n) + \alpha), \quad (1)$$

where d_a is the anchor sample, d_p and d_n are the positive and negative samples, respectively, α is the margin parameter (set to 1 in our experiments), and D denotes the distance metric. Specifically, we use the squared \mathcal{L}_2 norm:

$$D(d_1, d_2) = \left\| \frac{d_1}{\|d_1\|} - \frac{d_2}{\|d_2\|} \right\|^2. \quad (2)$$

Given a batch of N matching patch pairs from both modalities, $(\mathbf{x}_1^1, \mathbf{x}_1^2), \dots, (\mathbf{x}_N^1, \mathbf{x}_N^2)$, the network produces the corresponding descriptor pairs $(d_1^1, d_1^2), \dots, (d_N^1, d_N^2)$. For a given anchor, the positive sample is its paired descriptor, and the negative sample is a non-matching descriptor from the other modality.

4. GAP-VIR Dataset

Only a handful of paired multimodal patch datasets exist, leading to saturated results and limiting the exploration of key challenges such as domain transfer and domain adaptation. To advance research in multimodal patch matching,

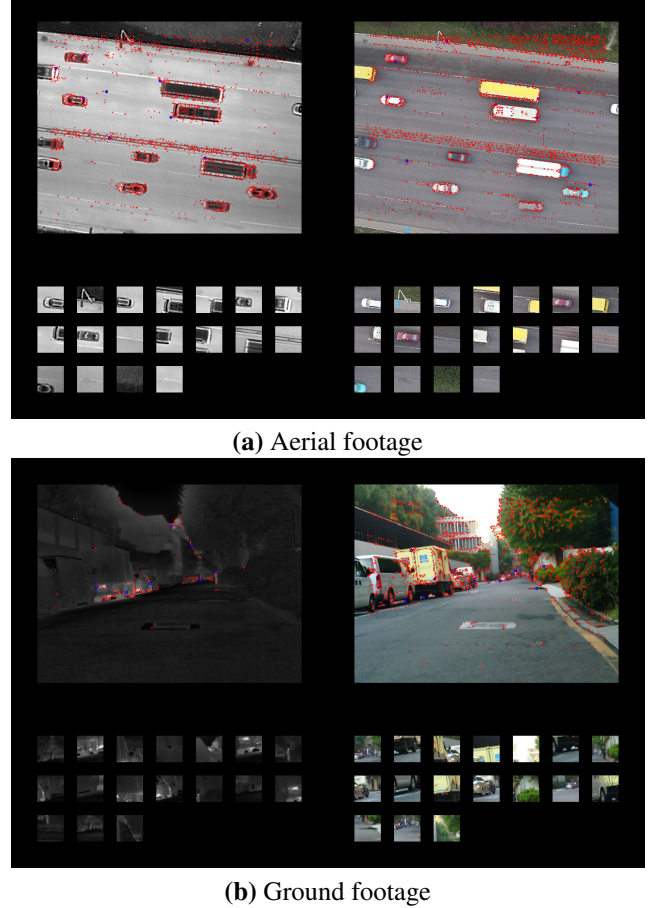


Figure 3. Patch extraction from paired aerial (a) and ground (b) imagery. Top: FAST keypoints (red) and selected keypoints (blue) overlaid on IR (left) and RGB (right) images. Bottom: corresponding 64×64 patches from both modalities. The detailed patch extraction procedure is provided in Supplementary Appendix A.

we introduce the **Ground Aerial Patch Vis-IR** (GAP-VIR) dataset, a new dataset of paired visible-infrared (VIS-IR) patches derived from cross-platform imagery. The dataset contains over 500K multimodal patches, both paired and unpaired, generated from 40K paired RGB and LWIR (thermal) images sourced from six existing datasets [22, 33, 43, 70–72], curated by Ran et al. [58] as part of the IR500K dataset. Full details of the patch-generation process are provided in Appendix A.

The images are divided into two categories: *Aerial* and *Ground-based* footage, yielding 270K and 235K patches, respectively. These categories differ not only in viewpoint, scene scale, and geometric distortions but also in resolution, level of detail, background clutter, and occlusion patterns. Moreover, camera and platform characteristics such as altitude, viewing angle, and motion further accentuate differences in both RGB and IR imagery. Examples are shown in Fig. 3, which presents paired RGB-IR images and their

Table 3. Patch matching FPR95 scores on the VIS-NIR benchmark [3]. Scores are reported for each category and the final mean. The best results are highlighted in **bold**.

Models	Field	Forest	Indoor	Mountain	Old Building	Street	Urban	Water	Mean
Traditional methods									
SIFT [46]	39.44	11.39	10.13	28.63	19.69	31.14	10.85	40.33	23.95
GISIFT [17]	34.75	16.63	10.63	19.52	12.54	21.80	7.21	25.78	18.60
LGHD [2]	16.52	3.78	7.91	10.66	7.91	6.55	7.21	12.76	9.16
Descriptor learning									
Q-Net [4]	17.01	2.70	6.16	9.61	4.61	3.99	2.83	8.44	6.86
L2-Net [73]	16.67	0.76	2.07	5.98	1.89	2.83	0.62	11.11	5.25
Exp-TLoss [82]	5.55	0.24	2.30	1.51	1.45	2.15	1.44	1.95	2.07
HardNet [50]	5.61	0.15	1.50	3.14	1.10	1.93	0.69	2.29	2.05
SOSNet [74]	5.94	0.13	1.53	2.45	0.99	2.04	0.78	1.90	1.97
D-Hybrid-CL [7]	4.40	0.20	2.48	1.50	1.19	1.93	0.78	1.56	1.70
Transformer-Encoder [51]	4.22	0.13	1.48	1.03	1.06	1.03	0.90	1.90	1.44
HyNet [75]	4.50	0.07	1.09	1.80	0.83	0.52	0.53	1.91	1.41
Hyp-Net (Ours)	3.97	0.13	0.83	0.76	0.74	0.53	0.39	1.51	1.11

extracted patches from aerial and ground footage, highlighting variations in scale and appearance. By introducing two distinct subsets with substantial differences, the dataset supports both training and evaluation of adaptation methods under varied domain shifts.

5. Experimental Results

We evaluate our approach on multimodal patch-matching datasets. These datasets consist of pairs of multimodal images and evaluation protocols that generate matching and non-matching patches. We compare our method against prior state-of-the-art approaches. Performance is measured using the false positive rate at 95% recall (FPR95), where lower values indicate better results.

5.1. Datasets

The VIS-NIR benchmark [3] contains 1.6 million pairs of visible and NIR 64×64 patches. It is divided into nine categories based on the VIS-NIR image sets from which the patches were derived. Following standard practice, only the first category, *Country*, is used for training and evaluation with an 80%–20% split. The remaining eight categories (field, forest, indoor, mountain, old building, street, urban, and water) are reserved for testing.

The En et al. [16] benchmark consists of patches derived from three multimodal datasets. VeDAI [59], a set of RGB and NIR images of environments and vehicles, was designed for vehicle detection in aerial imagery. The CUHK dataset [83] contains facial photographs paired with matching sketches, and RGB-NIR [8] consists of visible and NIR images. To extract patches and split the dataset into training, validation, and test sets, we follow the [51] protocol. The

Table 4. Patch matching FPR95 scores on the three datasets of the En et al. benchmark [16]. The best results are highlighted in **bold**.

Model	VEDAI	CUHK	RGB-NIR
SIFT [46]	42.74	5.87	32.53
MI-SIFT [49]	11.33	7.34	27.71
LGHD [2]	1.31	0.65	10.76
Siamese [3]	0.84	3.38	13.17
Pseudo-Siamese [3]	1.37	3.7	15.6
Q-Net [4]	0.78	0.9	22.5
TS-Net [10]	0.45	2.77	11.86
Transformer [51]	0	0.05	1.76
Hyp-Net (Ours)	0	0.03	1.39

VIS-LWIR benchmark, introduced by Aguilera et al. [3], is a patch dataset consisting of 21,370 pair samples extracted from aligned visible and long-wave infrared (LWIR) images. We follow the scheme of Yu et al. [86] for selecting non-matching patch pairs and for train-test separation, using an 80%-20% split. Unfortunately, we were unable to gain access to other datasets, such as the one introduced by Zhang [92], because we did not receive a response from the authors. In addition, we evaluated our models on the GAP-VIR dataset introduced in Section 4. We used the two patch categories, aerial and ground-based, to evaluate cross-domain adaptation. For each model, we trained on a single category, as well as on both categories combined. We then evaluated each model on the test set of each category.

5.2. Implementation Details

We trained the Siamese network from scratch using the Adam optimizer without weight decay, with parameters

Table 5. Patch matching FPR95 scores on the VIS-LWIR benchmark [3, 86] for descriptor-learning (left) and similarity-learning (right) methods. The best results are highlighted in **bold**. Our method matches the SOTA result reported by similarity-learning methods, despite their limited practicality.

Descriptor learning		Similarity learning	
Model	FPR95	Model	FPR95
MatchNet [21]	9.83	SCFDM [55]	1.89
Siamese [3]	13.89	MR-3A [57]	1.56
Pseudo-Siamese [3]	10.34	AFD-Net [56]	1.43
2-Channel [91]	8.34	MFD-Net [85]	0.97
Hyp-Net (Ours)	0.51	EFR-Net [87]	0.92
		FIL-Net [86]	0.69
		KGL-Net [88]	0.51

$\beta_1 = 0.9$ and $\beta_2 = 0.999$. We employed a reduce-on-plateau learning rate schedule, reducing the learning rate by a factor of 10 when the evaluation loss did not improve for three consecutive epochs. The learning rate started at $\eta_{max} = 10^{-2}$ and decayed to $\eta_{min} = 10^{-5}$. In addition, we applied a linear warm-up schedule of four epochs, starting at a learning rate of 0.25×10^{-2} before transitioning to the main schedule.

We repeated the learning rate schedule for four cycles, reinitializing the Adam optimizer at each cycle, following [68], which showed the benefit of cyclical over monotonically decreasing schedules. The cycles correspond to the negative sample mining strategies described in Section 3.3, with random sampling in the first cycle and hard negative mining in the remaining cycles. For the VIS-LWIR benchmark, we employed 12 cycles due to the smaller number of patches. This setup provides sufficient iterations for the model to adapt to augmentations and dropout without modifying other training parameters.

The augmentations used during training include random horizontal flips, random 90° rotations, and random vertical flips, all applied identically to both patches in a pair. In contrast, small random rotations of up to 5° and random gamma adjustments were applied independently to each patch in a pair. The first group was applied identically to both patches because the architecture, being relatively shallow, is sensitive to spatial position. The effects of the first augmentation group are evaluated in the ablation study (Table 8).

5.3. Results

In Table 3, we present our results on the VIS-NIR dataset, measured using the FPR95 metric. As discussed in Section 2.2, we restrict our evaluation to descriptor-learning methods, comparing against both traditional approaches [2, 17, 46] and recent deep learning methods [4, 7, 50, 51, 73–75, 82]. We demonstrate that our architecture significantly outperforms previous works by the overall mean score and

across most categories. We achieve a mean score of 1.11, improving upon the previous best of 1.41 and achieving up to a 30% reduction in FPR95 across some categories. As test performance fluctuates on unseen data, we report the score at the end of training.

The results on the En et al. [16] benchmark are shown in Table 4. We achieve a new improved state of the art (SOTA) FPR95 scores on the CUHK and NIR-RGB datasets, and match the zero FPR95 on VeDAI, previously reported in [51]. This outcome stems from the training and test sets in this dataset sharing similar distributions.

Table 5 presents results for the VIS-LWIR benchmark. In this benchmark, we show a substantial improvement over all descriptor-learning methods, reducing the FPR95 from 8.34 reported by Han et al. [21] to 0.51 (a 94% reduction). For reference, we also report recent scores for metric learning methods. Although metric learning methods enjoy a built-in advantage at inference, making them impractical at scale, our method achieves comparable performance to the recently reported SOTA by Yu et al. [88].

Table 6 presents GAP-VIR results from training on single or combined domains, with the former enabling cross-domain evaluation. We observe that Hyp-Net consistently outperforms the other models, achieving FPR95 improvements of 10%–60% across all domains except one. When examining cross-domain generalization, Hyp-Net trained on ground-based imagery outperforms other models on its own test set and when transferred to the *aerial* set. However, when trained on aerial imagery, both Hyp-Net and competing models struggle to generalize to ground data. This is likely due to substantial domain gap and the lower diversity of aerial patches, as illustrated in Fig. 3. Finally, when trained on both domains, attention-based models show significant improvements, suggesting that increased data diversity enhances generalization.

5.4. Ablation studies

Architectural Components. We conducted an ablation study on the architectural elements of Hyp-Net, and the results are shown in Table 8. We observe the best performance when all elements are used together, suggesting that they play complementary roles in the matching process. The addition of hypernetwork modules improves the FPR95 score by 17%, demonstrating their effectiveness in capturing relevant higher-order information. The architecture with CIN blocks outperforms those with IN and BN blocks by 7% and 14%, respectively. This provides evidence that IN blocks are more robust to appearance changes (as suggested in [56]), and that the modality-based information captured by CIN blocks is additionally beneficial. Random 90° rotation and vertical flip augmentations also improve the score by 9%, suggesting that encouraging rotation-invariant features enhances robustness on unseen data.

Table 6. Patch matching FPR95 scores for cross-domain evaluation on the GAP-VIR dataset. Models are trained separately on the ground set (170K), the aerial set (180K), and the combined set, and evaluated on each test set individually. HardNet++ denotes HardNet [50] with an enlarged architecture to match the number of convolutional channels in our model (see Table 2). The best results are shown in **bold**.

Model	Training Set: Ground		Training Set: Aerial		Training Set: Combined			
	Test Set	Ground	Aerial	Ground	Aerial	Ground	Aerial	Mean (combined)
HardNet++ [50]		3.94	6.10	12.28	2.04	4.39	2.09	3.24
Transformer [51]		3.83	5.94	15.43	1.82	1.86	1.13	1.50
Hyp-Net (Ours)		3.40	5.07	17.86	1.44	1.21	0.70	0.95

Table 7. Ablation study on backbone architectures for patch matching. *ViT Small* and *Swin Small* denote reduced versions with fewer layers, while *ResNet-18 L3* and *ResNet-18 L2* refer to ResNet-18 with only three or two residual layers, respectively. Architectural details are provided in Table 2 of Appendix B in the supplementary material. Results are reported as FPR95 scores on the VIS-NIR dataset, both per category and as overall means. Best results are shown in **bold**, and second-best in underline.

Model	Field	Forest	Indoor	Mountain	Old Building	Street	Urban	Water	Mean
VIT [13]	10.24	0.43	2.57	3.48	1.03	1.52	0.92	3.29	2.93
VIT Small	8.80	0.23	2.21	2.64	1.42	1.76	0.81	2.19	2.51
SWIN [44]	7.59	0.95	1.94	2.25	1.29	2.53	0.78	2.23	2.44
SWIN Small	<u>4.48</u>	0.12	1.08	1.05	0.91	1.14	0.63	1.63	1.38
ResNet-18	13.23	8.42	4.22	7.73	3.93	6.24	2.68	5.21	6.46
ResNet-18 L3	4.67	0.46	1.77	1.53	0.96	1.34	0.82	1.96	1.69
ResNet-18 L2	5.63	<u>0.11</u>	<u>1.04</u>	0.92	0.88	0.80	0.79	1.72	1.48
Hyp-Net Small	5.93	0.08	1.10	0.72	<u>0.82</u>	0.48	0.63	1.46	1.40
Hyp-Net Large	4.54	0.37	1.21	0.91	<u>0.82</u>	0.86	<u>0.48</u>	1.54	<u>1.34</u>
Hyp-Net (Ours)	3.97	0.13	0.83	<u>0.76</u>	0.74	<u>0.53</u>	0.39	<u>1.51</u>	1.11

Table 8. Ablation study of architectural elements: Patch matching FPR95 scores on the VIS-NIR dataset, where we vary a single architectural element at a time: augmentations, normalization blocks, or hypernetwork modules. The best result is highlighted in **bold**.

Ablation Check	Hypernet Model	Norm	90°		FPR95
			Rotation	Vertical Flip	
Augmentations	+	CIN	–		1.21
Normalization	+	BN	+		1.26
Normalization	+	IN	+		1.19
Architecture	–	CIN	+		1.30
Hyp-Net	+	CIN	+		1.11

Backbone. We conducted ablation studies to assess the effectiveness of different backbones on the VIS-NIR dataset, including ResNet [25], ViT [13], and Swin [44] Transformers. We also evaluated the effect of backbone size (layers and parameters), with full details provided in Appendix B. Results are shown in Table 7. First, we find that neither larger nor smaller convolutional backbones improve generalization, yielding FPR95 scores of 1.34 and 1.40, com-

pared to Hyp-Net’s 1.11. For ResNet-18, the full model performs poorly, but reducing depth improves results, with the two-layer reduction achieving an FPR score of 1.48.

ViT variants perform poorly overall, suggesting that despite their strong performance in other vision tasks, they may be less effective for generalization in patch matching. Swin performs better than ViT, with Swin Small reaching 1.38, slightly surpassing the previous SOTA of 1.41, though still behind Hyp-Net. Overall, these experiments indicate that (a) smaller networks up to a certain size generalize better, and (b) newer architectures do not necessarily improve performance on the diverse VIS-NIR test set.

6. Conclusion

We introduced Hyp-Net, a hypernetwork-based CNN architecture for multimodal patch matching, and GAP-VIR, a new RGB-IR patch dataset spanning both ground and aerial imagery. Our approach achieves state-of-the-art results on VIS-NIR, VIS-LWIR, and En et al. benchmark datasets, using an architecture comparable in size to previous solutions. Through ablation studies, we analyzed the role of backbone choice and observed that smaller CNNs tend to general-

ize better than standard-size CNNs and transformer-based models. GAP-VIR further enables evaluation under domain adaptation scenarios, providing a challenging benchmark for future research. We hope this work stimulates further research on cross-modal patch correspondence and broader multimodal matching tasks.

References

- [1] Cristhian Aguilera, Fernando Barrera, Felipe Lumbreras, Angel D. Sappa, and Ricardo Toledo. Multispectral image feature points. *Sensors*, 12(9):12661–12672, 2012. [2](#), [3](#)
- [2] Cristhian A. Aguilera, Angel D. Sappa, and Ricardo Toledo. LGHD: A feature descriptor for matching across non-linear intensity variations. In *IEEE Int. Conf. Image Process.*, pages 178–181, 2015. [2](#), [3](#), [6](#), [7](#)
- [3] Cristhian A. Aguilera, Francisco J. Aguilera, Angel D. Sappa, Cristhian Aguilera, and Ricardo Toledo. Learning cross-spectral similarity measures with deep convolutional neural networks. In *IEEE Conf. Comput. Vis. Pattern Recog. Worksh.*, pages 1–9, 2016. [2](#), [3](#), [6](#), [7](#), [13](#)
- [4] Cristhian A. Aguilera, Angel D. Sappa, Cristhian Aguilera, and Ricardo Toledo. Cross-spectral local descriptors via quadruplet network. *Sensors*, 17(4):873, 2017. [2](#), [3](#), [6](#), [7](#)
- [5] Vassileios Balntas, Edward Johns, Lilian Tang, and Krystian Mikolajczyk. PN-Net: Conjoined triple deep network for learning local image descriptors. *arXiv preprint arXiv:1601.05030*, 2016. [2](#), [3](#)
- [6] Vassileios Balntas, Edgar Riba, Daniel Ponsa, and Krystian Mikolajczyk. Learning local feature descriptors with triplets and shallow convolutional neural networks. In *Brit. Mach. Vis. Conf.*, page 3, 2016. [2](#), [3](#)
- [7] Elad Ben Baruch and Yosi Keller. Joint detection and matching of feature points in multimodal images. *IEEE Trans. Pattern Anal. Mach. Intell.*, 44(10):6585–6593, 2022. [2](#), [3](#), [6](#), [7](#), [14](#)
- [8] Matthew Brown and Sabine Süsstrunk. Multi-spectral SIFT for scene category recognition. In *IEEE Conf. Comput. Vis. Pattern Recog.*, pages 177–184, 2011. [6](#)
- [9] Vinod Kumar Chauhan, Jiandong Zhou, Ping Lu, Soheila Molaei, and David A. Clifton. A brief review of hypernetworks in deep learning. *arXiv preprint arXiv:2306.06955*, 2023. [4](#)
- [10] Jian Chen and Jie Tian. Real-time multi-modal rigid registration based on a novel symmetric-SIFT descriptor. *Progress in Natural Science*, 19(5):643–651, 2009. [2](#), [6](#)
- [11] Yinbo Chen and Xiaolong Wang. Transformers as meta-learners for implicit neural representations. In *Eur. Conf. Comput. Vis.*, pages 170–187. Springer, 2022. [4](#)
- [12] Jia Deng, Wei Dong, Richard Socher, Li-Jia Li, Kai Li, and Li Fei-Fei. ImageNet: A large-scale hierarchical image database. In *IEEE Conf. Comput. Vis. Pattern Recog.*, pages 248–255, 2009. [1](#)
- [13] Alexey Dosovitskiy, Lucas Beyer, Alexander Kolesnikov, Dirk Weissenborn, Xiaohua Zhai, Thomas Unterthiner, Mostafa Dehghani, Matthias Minderer, Georg Heigold, Sylvain Gelly, et al. An image is worth 16x16 words: Transformers for image recognition at scale. *arXiv preprint arXiv:2010.11929*, 2020. [2](#), [8](#), [14](#)
- [14] Zhaopeng Dou, Zhongdao Wang, Weihua Chen, Yali Li, and Shengjin Wang. Reliability-aware prediction via uncertainty learning for person image retrieval. In *Eur. Conf. Comput. Vis.*, pages 588–605. Springer, 2022. [1](#)
- [15] Vincent Dumoulin, Jonathon Shlens, and Manjunath Kudlur. A learned representation for artistic style. *arXiv preprint arXiv:1610.07629*, 2016. [2](#)
- [16] Sovann En, Alexis Lechervy, and Frédéric Jurie. TS-NET: Combining modality specific and common features for multimodal patch matching. In *IEEE Int. Conf. Image Process.*, pages 3024–3028, 2018. [2](#), [6](#), [7](#)
- [17] Damien Firmenichy, Matthew Brown, and Sabine Süsstrunk. Multispectral interest points for RGB-NIR image registration. In *IEEE Int. Conf. Image Process.*, pages 181–184, 2011. [2](#), [6](#), [7](#)
- [18] Xiyue Guo, Junjie Hu, Hujun Bao, and Guofeng Zhang. Descriptor distillation for efficient multi-robot slam. In *IEEE Int. Conf. Robot. Autom.*, pages 6210–6216, 2023. [1](#)
- [19] David Ha, Andrew Dai, and Quoc V. Le. Hypernetworks. *arXiv preprint arXiv:1609.09106*, 2016. [2](#), [4](#)
- [20] Boran Han, Shuai Zhang, Xingjian Shi, and Markus Reichstein. Bridging remote sensors with multisensor geospatial foundation models. In *IEEE Conf. Comput. Vis. Pattern Recog.*, pages 27852–27862, 2024. [3](#)
- [21] Xufeng Han, Thomas Leung, Yangqing Jia, Rahul Sukthankar, and Alexander C Berg. Matchnet: Unifying feature and metric learning for patch-based matching. In *IEEE Conf. Comput. Vis. Pattern Recog.*, pages 3279–3286, 2015. [2](#), [3](#), [7](#)
- [22] Zonghao Han, Ziye Zhang, Shun Zhang, Ge Zhang, and Shaohui Mei. Aerial visible-to-infrared image translation: Dataset, evaluation, and baseline. *J. Remote Sens.*, 3:0096, 2023. [5](#), [13](#), [14](#)
- [23] Chris Harris, Mike Stephens, et al. A combined corner and edge detector. In *Alvey Vision Conf.*, pages 10–5244. Manchester, UK, 1988. [13](#)
- [24] Mahmudul Hasan, Mark R. Pickering, and Xiuping Jia. Modified SIFT for multi-modal remote sensing image registration. In *IEEE Int. Geosci. Remote Sens. Symp.*, pages 2348–2351, 2012. [2](#)
- [25] Kaiming He, Xiangyu Zhang, Shaoqing Ren, and Jian Sun. Deep residual learning for image recognition. In *IEEE Conf. Comput. Vis. Pattern Recog.*, pages 770–778, 2016. [2](#), [8](#)
- [26] Xingyi He, Hao Yu, Sida Peng, Dongli Tan, Zehong Shen, Hujun Bao, and Xiaowei Zhou. MatchAnything: Universal cross-modality image matching with large-scale pre-training. *arXiv preprint arXiv:2501.07556*, 2025. [3](#)
- [27] Dan Hendrycks and Kevin Gimpel. Gaussian error linear units (gelus). *arXiv preprint arXiv:1606.08415*, 2016. [5](#)
- [28] Elad Hoffer and Nir Ailon. Deep metric learning using triplet network. In *Int. Workshop Similarity-Based Pattern Recogn.*, pages 84–92, Copenhagen, Denmark, 2015. Springer. [2](#), [3](#), [5](#)
- [29] Qibin Hou, Daquan Zhou, and Jiashi Feng. Coordinate attention for efficient mobile network design. In *IEEE Conf. Comput. Vis. Pattern Recog.*, pages 13713–13722, 2021. [3](#)

[30] Jie Hu, Li Shen, and Gang Sun. Squeeze-and-excitation networks. In *IEEE Conf. Comput. Vis. Pattern Recog.*, pages 7132–7141, 2018. 3

[31] Michal Irani and P Anandan. Robust multi-sensor image alignment. In *IEEE Int. Conf. Comput. Vis.*, pages 959–966, 1998. 1, 2

[32] Michael Jahrer, Michael Grabner, and Horst Bischof. Learned local descriptors for recognition and matching. In *Comput. Vis. Winter Workshop*, pages 103–118, 2008. 2

[33] Xinyu Jia, Chuang Zhu, Minzhen Li, Wenqi Tang, and Wenli Zhou. LLVIP: A visible-infrared paired dataset for low-light vision. In *IEEE Int. Conf. Comput. Vis.*, pages 3496–3504, 2021. 5, 13, 14

[34] Xingyu Jiang, Jiayi Ma, Guobao Xiao, Zhenfeng Shao, and Xiaojie Guo. A review of multimodal image matching: Methods and applications. *Inf. Fusion*, 73:22–71, 2021. 2

[35] Yosi Keller and Amir Averbuch. Robust multi-sensor image registration using pixel migration. In *IEEE Sensor Array Multich. Signal Process. Workshop*, pages 100–104, 2002. 2

[36] Yosi Keller and Amir Averbuch. Multisensor image registration via implicit similarity. *IEEE Trans. Pattern Anal. Mach. Intell.*, 28(5):794–801, 2006. 2

[37] Seungryong Kim, Dongbo Min, Bumsuk Ham, Seungchul Ryu, Minh N. Do, and Kwanghoon Sohn. DASC: Dense adaptive self-correlation descriptor for multi-modal and multi-spectral correspondence. In *IEEE Conf. Comput. Vis. Pattern Recog.*, pages 2103–2112, 2015. 3

[38] Yeongmin Ko, Yong-Jun Jang, Vinh Quang Dinh, Hae-Gon Jeon, and Moongu Jeon. Spectral-invariant matching network. *Inf. Fusion*, 91:623–632, 2023. 2, 3

[39] Vijay Kumar BG, Gustavo Carneiro, and Ian Reid. Learning local image descriptors with deep siamese and triplet convolutional networks by minimising global loss functions. In *IEEE Conf. Comput. Vis. Pattern Recog.*, pages 5385–5394, 2016. 3

[40] Benny Kupfer, Nathan S. Netanyahu, and Ilan Shimshoni. An efficient SIFT-based mode-seeking algorithm for sub-pixel registration of remotely sensed images. *IEEE Geosci. Remote Sens. Lett.*, 12(2):379–383, 2014. 2

[41] Jacqueline Le Moigne, Arlene A. Cole-Rhodes, Roger D. Eastman, Nathan S. Netanyahu, Harold S. Stone, Ilya Zavorin, and Jeffrey T. Morisette. Multitemporal and multi-sensor image registration. In *Image Registration for Remote Sensing*, Jacqueline Le Moigne, Nathan S. Netanyahu and Roger D. Eastman (Eds.), pages 293–338. Cambridge University Press, 2011. 2

[42] Gidi Littwin and Lior Wolf. Deep meta functionals for shape representation. In *IEEE Int. Conf. Comput. Vis.*, pages 1824–1833, 2019. 4

[43] Jinyuan Liu, Xin Fan, Zhanbo Huang, Guanyao Wu, Risheng Liu, Wei Zhong, and Zhongxuan Luo. Target-aware dual adversarial learning and a multi-scenario multi-modality benchmark to fuse infrared and visible for object detection. In *IEEE Conf. Comput. Vis. Pattern Recog.*, pages 5802–5811, 2022. 5, 13, 14

[44] Ze Liu, Yutong Lin, Yue Cao, Han Hu, Yixuan Wei, Zheng Zhang, Stephen Lin, and Baining Guo. Swin transformer: Hierarchical vision transformer using shifted windows. In *IEEE Int. Conf. Comput. Vis.*, pages 10012–10022, 2021. 2, 8, 14

[45] Ilya Loshchilov and Frank Hutter. SGDR: Stochastic gradient descent with warm restarts. *arXiv preprint arXiv:1608.03983*, 2016. 14

[46] David G. Lowe. Distinctive image features from scale-invariant keypoints. *Int. J. Comput. Vis.*, 60(2):91–110, 2004. 2, 6, 7

[47] Shahar Lutati and Lior Wolf. OCD: Learning to overfit with conditional diffusion models. In *Int. Conf. Mach. Learn.*, pages 23157–23169, 2023. 4

[48] Jiayi Ma, Xingyu Jiang, Aoxiang Fan, Junjun Jiang, and Junchi Yan. Image matching from handcrafted to deep features: A survey. *Int. J. Comput. Vis.*, 129(1):23–79, 2021. 3

[49] Rui Ma, Jian Chen, and Zhong Su. MI-SIFT: Mirror and in-version invariant generalization for SIFT descriptor. In *ACM Int. Conf. Image Video Retrieval*, pages 228–235, 2010. 2, 6

[50] Anastasiia Mishchuk, Dmytro Mishkin, Filip Radenovic, and Jiri Matas. Working hard to know your neighbor’s margins: Local descriptor learning loss. *Adv. Neural Inform. Process. Syst.*, 30, 2017. 2, 3, 6, 7, 8, 14

[51] Aviad Moreshet and Yosi Keller. Paying attention to multiscale feature maps in multimodal image matching. *arXiv preprint arXiv:2103.11247*, 2021. 2, 3, 4, 6, 7, 8, 14

[52] Nathan S. Netanyahu, Jacqueline Le Moigne, and Jeffrey G Masek. Georegistration of Landsat data via robust matching of multiresolution features. *IEEE Trans. Geosci. Remote Sens.*, 42(7):1586–1600, 2004. 2

[53] Yuval Nirkin, Lior Wolf, and Tal Hassner. HyperSeg: Patchwise hypernetwork for real-time semantic segmentation. In *IEEE Conf. Comput. Vis. Pattern Recog.*, pages 4061–4070, 2021. 4

[54] James Philbin, Ondrej Chum, Michael Isard, Josef Sivic, and Andrew Zisserman. Object retrieval with large vocabularies and fast spatial matching. In *IEEE Conf. Comput. Vis. Pattern Recog.*, pages 1–8, 2007. 1

[55] Dou Quan, Shuai Fang, Xuefeng Liang, Shuang Wang, and Licheng Jiao. Cross-spectral image patch matching by learning features of the spatially connected patches in a shared space. In *Asian Conf. Comput. Vis.*, pages 115–130. Springer, 2019. 7

[56] Dou Quan, Xuefeng Liang, Shuang Wang, Shaowei Wei, Yanfeng Li, Ning Huyan, and Licheng Jiao. AFD-Net: Aggregated feature difference learning for cross-spectral image patch matching. In *IEEE Int. Conf. Comput. Vis.*, pages 3017–3026, 2019. 2, 3, 7

[57] Dou Quan, Shuang Wang, Yi Li, Bowu Yang, Ning Huyan, Jocelyn Chanussot, Biao Hou, and Licheng Jiao. Multi-relation attention network for image patch matching. *IEEE Trans. Image Process.*, 30:7127–7142, 2021. 3, 7

[58] Lingyan Ran, Lidong Wang, Guangcong Wang, Peng Wang, and Yanning Zhang. DiffV2IR: visible-to-infrared diffusion model via vision-language understanding. *arXiv preprint arXiv:2503.19012*, 2025. 3, 5, 13

[59] Sebastien Razakarivony and Frederic Jurie. Vehicle detection in aerial imagery: A small target detection benchmark. *J. Vis. Commun. Image Represent.*, 34:187–203, 2016. 6

[60] Jiangwei Ren, Xingyu Jiang, Zizhuo Li, Dingkang Liang, Xin Zhou, and Xiang Bai. MINIMA: Modality invariant image matching. *arXiv preprint arXiv:2412.19412*, 2024. 3

[61] Edward Rosten, Reid Porter, and Tom Drummond. Faster and better: A machine learning approach to corner detection. *IEEE Trans. Pattern Anal. Mach. Intell.*, 32(1):105–119, 2008. 13

[62] Ethan Rublee, Vincent Rabaud, Kurt Konolige, and Gary Bradski. ORB: An efficient alternative to SIFT or SURF. In *IEEE Int. Conf. Comput. Vis.*, pages 2564–2571, 2011. 13

[63] Eli Shechtman and Michal Irani. Matching local self-similarities across images and videos. In *IEEE Conf. Comput. Vis. Pattern Recog.*, pages 1–8, 2007. 3

[64] Yifei Shi, Kai Xu, Matthias Niessner, Szymon Rusinkiewicz, and Thomas Funkhouser. PlaneMatch: Patch coplanarity prediction for robust RGB-D reconstruction. In *Eur. Conf. Comput. Vis.*, pages 750–766, 2018. 1

[65] Edgar Simo-Serra, Eduard Trulls, Luis Ferraz, Iasonas Kokkinos, Pascal Fua, and Francesc Moreno-Noguer. Discriminative learning of deep convolutional feature point descriptors. In *IEEE Int. Conf. Comput. Vis.*, pages 118–126, 2015. 2, 3

[66] Saurabh Singh and Shankar Krishnan. Filter response normalization layer: Eliminating batch dependence in the training of deep neural networks. In *IEEE Conf. Comput. Vis. Pattern Recog.*, pages 11237–11246, 2020. 3

[67] Vincent Sitzmann, Julien Martel, Alexander Bergman, David Lindell, and Gordon Wetzstein. Implicit neural representations with periodic activation functions. *Adv. Neural Inform. Process. Syst.*, 33:7462–7473, 2020. 4

[68] Leslie N. Smith. Cyclical learning rates for training neural networks. In *IEEE Workshop Applications Comput. Vis.*, pages 464–472, 2017. 7

[69] Aristeidis Sotiras, Christos Davatzikos, and Nikos Paragios. Deformable medical image registration: A survey. *IEEE Trans. Med. Imaging*, 32(7):1153–1190, 2013. 1

[70] Yiming Sun, Bing Cao, Pengfei Zhu, and Qinghua Hu. Drone-based RGB-infrared cross-modality vehicle detection via uncertainty-aware learning. *IEEE Trans. Circuit Syst. Video Technol.*, 32(10):6700–6713, 2022. 5, 13, 14

[71] Linfeng Tang, Jiteng Yuan, Hao Zhang, Xingyu Jiang, and Jiayi Ma. PIAFusion: A progressive infrared and visible image fusion network based on illumination aware. *Inf. Fusion*, 83:79–92, 2022. 13, 14

[72] Teledyne FLIR. Free expanded flir thermal dataset for adas and autonomous vehicle testing. <https://oem.flir.com/solutions/automotive/dataset/>, 2022. Accessed: 2025-09-22. 5, 13, 14

[73] Yurun Tian, Bin Fan, and Fuchao Wu. L2-Net: Deep learning of discriminative patch descriptor in euclidean space. In *IEEE Conf. Comput. Vis. Pattern Recog.*, pages 661–669, 2017. 2, 3, 6, 7

[74] Yurun Tian, Xin Yu, Bin Fan, Fuchao Wu, Huub Heijnen, and Vassileios Balntas. SOSNet: Second order similarity regularization for local descriptor learning. In *IEEE Conf. Comput. Vis. Pattern Recog.*, pages 11016–11025, 2019. 3, 6, 14

[75] Yurun Tian, Axel Barroso Laguna, Tony Ng, Vassileios Balntas, and Krystian Mikolajczyk. HyNet: Learning local descriptor with hybrid similarity measure and triplet loss. *Adv. Neural Inform. Process. Syst.*, 33:7401–7412, 2020. 3, 6, 7, 14

[76] Önder Tuzcuoğlu, Aybora Köksal, Buğra Sofu, Sinan Kalkan, and A. Aydin Alatan. XoFTR: Cross-modal feature matching transformer. In *IEEE Conf. Comput. Vis. Pattern Recog.*, pages 4275–4286, 2024. 3

[77] Tomer Volk, Eyal Ben-David, Ohad Amosy, Gal Chechik, and Roi Reichart. Example-based hypernetworks for multi-source adaptation to unseen domains. In *Findings Assoc. Comput. Linguist.*, pages 9096–9113, 2023. 4

[78] Johannes Von Oswald, Christian Henning, Benjamin F. Grewe, and João Sacramento. Continual learning with hypernetworks. *arXiv preprint arXiv:1906.00695*, 2019. 4

[79] Oleg Voynov, Gleb Bobrovskikh, Pavel Karpyshev, Saveliy Galochkin, Andrei-Timotei Ardelean, Arseniy Bozhenko, Ekaterina Karmanova, Pavel Kopanov, Yaroslav Labutin-Rymsho, Ruslan Rakhimov, Aleksandr Safin, Valerii Serpiva, Alexey Artemov, Evgeny Burnaev, Dzmitry Tsetserukou, and Denis Zorin. Multi-sensor large-scale dataset for multi-view 3D reconstruction. In *IEEE Conf. Comput. Vis. Pattern Recog.*, pages 21392–21403, 2023. 3

[80] Han Wang, Shengyang Li, Jian Yang, Yuxuan Liu, Yixuan Lv, and Zhuang Zhou. Cross-modal ship re-identification via optical and SAR imagery: A novel dataset and method. *arXiv preprint arXiv:2506.22027*, 2025. 3

[81] Shuang Wang, Dou Quan, Xuefeng Liang, Mengdan Ning, Yanhe Guo, and Licheng Jiao. A deep learning framework for remote sensing image registration. *ISPRS J. Photogramm. Remote Sens.*, 145:148–164, 2018. 1

[82] Shuang Wang, Yanfeng Li, Xuefeng Liang, Dou Quan, Bowu Yang, Shaowei Wei, and Licheng Jiao. Better and faster: Exponential loss for image patch matching. In *IEEE Int. Conf. Comput. Vis.*, pages 4812–4821, 2019. 2, 3, 6, 7

[83] Xiaogang Wang and Xiaoou Tang. Face photo-sketch synthesis and recognition. *IEEE Trans. Pattern Anal. Mach. Intell.*, 31(11):1955–1967, 2008. 6

[84] Yuanxin Ye, Bai Zhu, Tengfeng Tang, Chao Yang, Qizhi Xu, and Guo Zhang. A robust multimodal remote sensing image registration method and system using steerable filters with first-and second-order gradients. *ISPRS J. Photogramm. Remote Sens.*, 188:331–350, 2022. 1, 3

[85] Chuang Yu, Yunpeng Liu, Chenxi Li, Lin Qi, Xin Xia, Tianci Liu, and Zhuhua Hu. Multibranch feature difference learning network for cross-spectral image patch matching. *IEEE Trans. Geosci. Remote Sens.*, 60:1–15, 2022. 2, 3, 7

[86] Chuang Yu, Yunpeng Liu, Jinmiao Zhao, Shuhang Wu, and Zhuhua Hu. Feature interaction learning network for cross-spectral image patch matching. *IEEE Trans. Image Process.*, 32:5564–5579, 2023. 2, 6, 7

[87] Chuang Yu, Jinmiao Zhao, Yunpeng Liu, Shuhang Wu, and Chenxi Li. Efficient feature relation learning network for

cross-spectral image patch matching. *IEEE Trans. Geosci. Remote Sens.*, 61:1–17, 2023. 3, 7

[88] Chuang Yu, Yunpeng Liu, Jinmiao Zhao, and Xiangyu Yue. Why and how: Knowledge-guided learning for cross-spectral image patch matching. *arXiv preprint arXiv:2412.11161*, 2024. 3, 7

[89] Chuang Yu, Yunpeng Liu, Jinmiao Zhao, Dou Quan, Zelin Shi, and Xiangyu Yue. Relational representation learning network for cross-spectral image patch matching. *Inf. Fusion*, page 103749, 2025. 2, 3

[90] Hao Yu, Xu Cheng, Wei Peng, Weihao Liu, and Guoying Zhao. Modality unifying network for visible-infrared person re-identification. In *IEEE Int. Conf. Comput. Vis.*, pages 11185–11195, 2023. 3

[91] Sergey Zagoruyko and Nikos Komodakis. Learning to compare image patches via convolutional neural networks. In *IEEE Conf. Comput. Vis. Pattern Recog.*, pages 4353–4361, 2015. 2, 3, 7

[92] Xiuwei Zhang, Yanping Li, Zhaoshuai Qi, Yi Sun, and Yanning Zhang. Learning multi-domain feature relation for visible and long-wave infrared image patch matching. *arXiv preprint arXiv:2308.04880*, 2023. 3, 6

[93] Xiuwei Zhang, Yi Sun, Yamin Han, Yanping Li, Hanlin Yin, Yinghui Xing, and Yanning Zhang. SSML-QNet: scale-separative metric learning quadruplet network for multi-modal image patch matching. In *Int. Joint Conf. Artif. Intell.*, pages 4593–4601, 2023. 3

[94] Rufan Zhou, Dou Quan, Chonghua Lv, Yanhe Guo, Shuang Wang, Yu Gu, and Licheng Jiao. Deep continuous matching network for more robust multi-modal remote sensing image patch matching. In *IEEE Int. Geosci. Remote Sens. Symp.*, pages 6057–6060, 2023. 3

[95] Bai Zhu, Chao Yang, Jinkun Dai, Jianwei Fan, Yao Qin, and Yuanxin Ye. R2FD2: fast and robust matching of multimodal remote sensing images via repeatable feature detector and rotation-invariant feature descriptor. *IEEE Trans. Geosci. Remote Sens.*, 61:1–15, 2023. 3

Supplementary Material

A. GAP-VIR Dataset Generation

As introduced in Sec. IV, GAP-VIR is a dataset of paired VIS-IR patches derived from cross-platform imagery. Here, we provide additional details on its construction. The patches were created from 40K paired VIS-IR images of the IR500K dataset introduced by Ran et al. [58]. IR500K is composed of multiple infrared and visible image datasets, from which we used a subset of paired images captured by ground-based and aerial RGB and LWIR (thermal) cameras. Table 9 summarizes the six original paired multimodal datasets [22, 33, 43, 70–72]. Table 9 summarizes the paired multimodal datasets used to construct our patch dataset, including imaging platform, acquisition type, and splitting protocols. We also indicate whether grouping information was available to guide data diversity and whether cross-frame duplicate removal was applied.

Our split protocol is designed to minimize the risk of similarity leakage between train and test sets by taking into account acquisition type, grouping, and sequential order. All datasets were divided using a 70%/10%/20% train/validation/test ratio, with grouping applied first where relevant. For LLVIP [33], whose data are organized into sets of frames from individual static cameras, we grouped by camera so that all frames from the same camera remained in a single split. For MSRS [71], image filenames include a day/night indicator; we first separated the dataset into daily and nightly subsets and then split each subset sequentially into train, validation, and test. This choice was motivated by M3FD [43], which also contains daily and nightly imagery but lacks explicit indicators for separation. After applying these grouping rules, all splits were finalized using sequential (lexical) file order, ensuring consistent treatment across datasets. These steps together help prevent visually similar or identical patches from appearing in both training and test sets.

After defining the dataset splits, we turn to the process of patch extraction. Several factors must be considered when extracting multimodal patches: spectral differences, detector robustness, feature bias (e.g., foliage), and duplicate removal. Details on these aspects are scarce in the literature, with prior work typically providing only high-level descriptions [3]. We therefore introduce a detailed patch-level extraction procedure tailored for multimodal datasets. We detect keypoints independently per modality using FAST [61] and rank them by the Harris corner score [23]. To reduce spatial redundancy, we group keypoints into 16×16 cells and retain only those that are present (or have neighbors) in both modalities. For 64×64 patches, we apply non-maximum suppression (NMS) both within each modality and across modalities. For LLVIP static-camera sets, we further de-duplicate patches across frames by discarding

Algorithm 1 Cross-spectral patch extraction per image pair

```

1: Input: Paired images  $I^{(a)}, I^{(b)}$ ; patch size  $P=64$ ; grid
   cell size  $g=16$ ; margin  $m=P/2$ ; Harris threshold factor
    $\tau_H$ ; intra-/inter-modality IoU thresholds  $t_{\text{intra}}, t_{\text{inter}}$ ;
   target patches per pair  $N$ 
2: Output: Selected patch set  $\mathcal{S}$ 
3: for  $u \in \{a, b\}$  do ▷ Per modality
4:    $R \leftarrow \text{HARRIS}(I^{(u)})$ ;  $K^{(u)} \leftarrow$ 
   FASTDETECT( $I^{(u)}$ ); set  $k.\text{score} \leftarrow R(k)$  for all
    $k \in K^{(u)}$ 
5:   Remove edge points: delete  $k \in K^{(u)}$  with border
   distance  $< m$ 
6:   Remove low-score points: let  $s_{\text{max}} \leftarrow$ 
    $\max_{k \in K^{(u)}} k.\text{score}$ ; delete any  $k$  with  $k.\text{score} <$ 
    $\tau_H s_{\text{max}}$ 
7:   Partition and keep top per cell: divide image into
    $g \times g$  cells; in each cell, retain only the highest-score
   keypoint
8:    $C^{(u)} \leftarrow \{\text{CELL}(k) \mid k \in K^{(u)}\}$  ▷ Cells occupied
   after filtering
9: end for
10:  $C \leftarrow \mathcal{N}_{3 \times 3}(C^{(a)}) \cap \mathcal{N}_{3 \times 3}(C^{(b)})$  ▷ Expand
   each cell to its 8 neighbors (Moore neighborhood) and
   intersect modalities
11: for  $u \in \{a, b\}$  do
12:   Cross-modal consistency: keep only  $k \in K^{(u)}$ 
   with  $\text{CELL}(k) \in C$ 
13:   Extract a  $P \times P$  patch around each  $k \in K^{(u)}$  to
   form  $\mathcal{P}^{(u)}$ 
14:   Intra-modal NMS: scan  $\mathcal{P}^{(u)}$  by descending score;
   retain a patch if its IoU with all kept patches is  $< t_{\text{intra}}$ 
15:   Sort  $\mathcal{P}^{(u)}$  by score; select  $\lfloor N/4 \rfloor$  top patches and
   sample  $\lceil N/4 \rceil$  additional ones without replacement
   from the remainder
16: end for
17: Optional de-duplication (static frames): per modality,
   compare each patch's ORB descriptor against
   patches from previous frames in the same or neighbor-
   ing grid cell; discard the patch if a close match is found,
   otherwise keep it in the cache
18:  $\mathcal{S} \leftarrow \mathcal{P}^{(a)} \cup \mathcal{P}^{(b)}$ 
19: Inter-modal NMS: remove any patch in  $\mathcal{S}$  whose IoU
   with a higher-scoring kept patch is  $\geq t_{\text{inter}}$ 
20: return  $\mathcal{S}$ 

```

those whose ORB descriptors [62] match those already included. The complete cross-spectral patch extraction procedure is given in Algorithm 1.

Table 9. Summary of paired multimodal datasets used to construct our multimodal patch dataset. For each dataset, we report the imaging platform (ground or aerial), the number of paired samples, acquisition type, availability of grouping information (e.g., by camera or time of day) for diversity in splits, the protocol for train/validation/test division, and whether cross-frame duplicate patch removal was applied.

Dataset Name	Imaging Platform	Number of Image Pairs	Acquisition Type	Existing Grouping	Data Split Protocol	Patch Deduplication
AVIID [22]	Aerial	1,280	Continuous Video	-	Sequential	-
Visdrone [70]	Aerial	13,442	Multi-Scene Frames	Train/Val/Test	Already Split	-
LLVIP [33]	Ground	15,488	Fixed-Camera Frame Sets	Camera Sets	Camera sets	+
FLIR [72]	Ground	5,142	Sampled Video Frames	-	Sequential	-
M3FD [43]	Ground	4,200	Multi Scene Frames	-	Sequential	-
MSRS [71]	Ground	1,444	Multi Scene Frames	Day/Night	Day/Night Sequential	-

Table 10. Backbone architectures used in the ablation study. We compare structural details of ResNet-18, ViT, Swin Transformer, and our custom CNN backbones (standard, small, and large variants). *ViT Small* and *Swin Small* are reduced versions with fewer layers, while *ResNet-18 L3* and *ResNet-18 L2* use only three or two residual layers, respectively. The *Embedding Channels* column reports the embedding size for Transformers and the output channels of the final CNN layer.

MODEL	HYPERNET MODULE	NORM	LAYERS	EMBEDDING CHANNELS	NUM HEADS	WINDOW SIZE	PATCH SIZE	NUM PARAMETERS
ViT [13]	-	LN	12	768	12	-	16	51,942,784
ViT SMALL	-	LN	6	768	12	-	16	26,730,880
SWIN [44]	-	LN	[2,2,6,2]	384	[3,6,12,24]	[4,4,4,2]	4	27,893,994
SWIN SMALL	-	LN	[2,1,1]	384	[3,6,12]	[8,4,4]	4	3,614,296
RESNET-18	-	BN	17	512	-	-	-	11,442,388
RESNET-18 L3	-	BN	13	256	-	-	-	3,305,679
RESNET-18 L2	-	BN	9	128	-	-	-	2,240,690
HYP-NET SMALL	+	CIN	6	128	-	-	-	1,350,435
HYP-NET LARGE	+	CIN	10	256	-	-	-	4,111,206
HYP-NET (OURS)	+	CIN	8	128	-	-	-	1,662,820

B. Alternative Backbones

As discussed in Sec. V-D, our ablation studies compared CNN and Transformer architectures using both standard and custom backbones. Table 10 summarizes all tested backbone configurations. For the standard CNN backbone underlying Hyp-Net, similar in structure and size to those used in prior work [7, 50, 51, 74, 75], we created larger and smaller variants by adding or removing two layers, respectively. For a ResNet backbone, we used the compact ResNet-18, which consists of four residual blocks with two convolutions each. We created three variants with four, three, and two residual blocks, the smallest having a parameter count comparable to the standard CNN backbone. All variants were trained using the same protocol described in Sec. V-B.

When using default Transformer architectures with a nonstandard patch size (64×64 instead of the usual $224 \times$

224), some adjustments were unavoidable. We adapted the positional encodings accordingly and modified the local window size for the Swin architecture. Given that our Hyp-Net CNN has far fewer parameters than ViT and Swin, we also introduced smaller variants (*ViT Small* and *Swin Small*). We did not extend the Transformer architectures with hypernetworks, as they already include built-in attention mechanisms. For training the ViT and Swin architectures, we largely followed the procedures in Section 5.2, with minor modifications. In particular, we used a cosine annealing scheduler [45] with a 50-epoch cycle for the smaller variants but only 2 epochs for the standard Transformer architectures.